Characterization and Syngas Production at Low Temperature via Dry Reforming of Methane over Ni-M (M = Fe, Cr) Catalysts Tailored from LDH Structure

Manel Hallassi, Rafik Benrabaa, Nawal Fodil Cherif, Djahida Lerari, Redouane Chebout, Khaldoun Bachari, Annick Rubbens, Pascal Roussel, Rose-Noelle Vannier, Martine Trentesaux, et al.

Characterization and Syngas Production at Low Temperature via Dry Reforming of Methane over Ni-M (M = Fe, Cr) Catalysts Tailored from LDH Structure

Manel Hallassi [1,2,3], Rafik Benrabaa [2,4], Nawal Fodil Cherif [5], Djahida Lerari [5], Redouane Chebout [5], Khaldoun Bachari [5], Annick Rubbens [3], Pascal Roussel [3], Rose-Noëlle Vannier [3], Martine Trentesaux [3] and Axel Löfberg [3,*]

1   Département de Génie des Procédés, Faculté de Technologie, Université 20 Août-Skikda, BP 26, Route Al-Hadaiek, El Hadaik 21000, Skikda, Algeria
2   Laboratoire de Physico-Chimie des Matériaux, Faculté des Sciences et de la Technologie, Université Chadli Bendjedid-El Tarf, BP 73, El Tarf 36000, Algiers, Algeria
3   Univ. Lille, CNRS, Centrale Lille, Univ. Artois, UMR 8181-UCCS-Unité de Catalyse et Chimie du Solide, F-59000 Lille, France
4   Laboratoire de Matériaux Catalytiques et Catalyse en Chimie Organique, Faculté de Chimie, Université des Sciences et de la Technologie Houari Boumediene, BP 32, El-Alia, Bab Ezzouar 16111, Alger, Algeria
5   Centre de Recherche Scientifique et Technique en Analyses Physico-Chimiques, BP 384, Siège ex-Pasna Zone Industrielle, Bou-Ismail 42004, Tipaza, Algeria
*   Correspondence: axel.lofberg@univ-lille.fr; Tel.: +33-03-20-43-45-27

Abstract: Bimetallic layered double oxide (LDO) NiM (M = Cr, Fe) catalysts with nominal compositions of Ni/M = 2 or 3 were tailored from layered double hydroxides (LDH) using a coprecipitation method to investigate the effects of the trivalent metal (Cr or Fe) and the amount of Ni species on the structural, textural, reducibility, and catalytic properties for CH_4/CO_2 reforming. The solids before (LDH) and after (LDO) thermal treatment at 500 °C were characterized using TGA-TD-SM, HT-XRD, XRD, Raman, and IR-ATR spectroscopies; N_2 physical adsorption; XPS; and H_2-TPR. According to the XRD and Raman analysis, a hydrotalcite structure was present at room temperature and stable up to 250 °C. The interlayer space decreased when the temperature increased, with a lattice parameter and interlayer space of 3.018 Å and 7.017 Å, respectively. The solids fully decomposed into oxide after calcination at 500 °C. NiO and spinel phases (NiM_2O_4, M = Cr or Fe) were observed in the NiM (M = Cr, Fe) catalysts, and Cr_2O_3 was detected in the case of NiCr. The NiFe catalysts show low activity and selectivity for DRM in the temperature range explored. In contrast, the chromium compound demonstrated interesting CH_4 and CO_2 conversions and generally excellent H_2 selectivity at low reaction temperatures. CH_4 and CO_2 conversions of 18–20% with H_2/CO of approx. 0.7 could be reached at temperatures as low as 500 °C, but transient behavior and deactivation were observed at higher temperatures or long reaction times. The excellent activity observed during this transient sequence was attributed to the stabilization of the metallic Ni particles formed during the reduction of the NiO phase due to the presence of $NiCr_2O_4$, opening the path for the use of these materials in periodic or looping processes for methane reforming at low temperature.

Keywords: H_2 production; Ni-(Fe/Cr); layered double hydroxide; CO_2 reforming

1. Introduction

The catalytic reactions for the transformation of natural gas into synthesis gas (CO + H_2) are currently highly strategic industrial targets for the production of alternative liquid fuels. One interesting way to valorize methane is through the dry reforming of methane (DRM), which is undertaken in the presence of carbon dioxide (CO_2) [1,2]. This

process is mainly endothermic [3], and CO_2 is used as the oxidizing agent, as shown in the following equation:

$$CH_4 + CO_2 \rightarrow 2\,CO + 2H_2 \; ; \; \Delta H_{298\,K} = +247\;kJ/mol, \tag{1}$$

DRM is of particular interest because it converts two greenhouse pollutant gases, CH_4 and CO_2, into synthesis gas or hydrogen, which can subsequently be converted into valuable chemicals [4]. The methane reforming reaction is commonly carried out in the presence of supported noble metal (Rh, Pt, and Pd) or nickel metal [5] catalysts. Noble metals show better resistance to coke formation, but nickel is known to be a less expensive metal, with great reactivity in reforming processes [3–5]. However, one of the major issues associated with CO_2 reforming is the rapid carbon deposition on the catalyst, which mainly results from the carbon monoxide dissociation (reaction (2)) and/or the methane decomposition (reaction (3)) [6]. This coke deposition brings a progressive catalyst deactivation.

$$2\,CO \rightarrow CO_2 + C, \tag{2}$$

$$CH_4 \rightarrow C + 2\,H_2, \tag{3}$$

To limit sintering and reduce coke formation, the stabilization of the particles at a nanoscale level is necessary. Among the various solutions available to increase metal particle dispersion on the catalyst surface, one consists in incorporating the active phase as a well-defined structure, such as a spinel, a perovskite, or a pyrochlore [7–10]. However, new classes of porous solids that can be used to obtain solid catalysts with high specific surface areas for DRM are being studied and investigated. Many studies have been published, or are still ongoing, on the design of efficient, more stable, and eco-friendly catalysts [11]. Among the various types of materials, layered double hydroxides (LDH) containing transition metals as active components seem to be good candidates for the dry reforming of methane [12,13]. Indeed, the interest in LDHs relates to their two-dimensional character, appropriate alkalinity and ability to form, through calcination, oxides with homogeneous mesoporous textures and proper specific surface areas. LDH materials are therefore desirable precursors for catalysts [14,15].

Thus, on one hand, this work was dedicated to the preparation of an efficient Ni-transition metal bimetallic catalyst for DRM. On the other hand, the reactivity in the CO_2 reforming reaction of two bimetallic catalysts based on nickel–iron (Ni-Fe) and nickel–chromium (Ni-Cr) compositions was investigated. The bimetallic catalysts were built up at 500 °C from LDH precursors. These latter were obtained through a coprecipitation method with Ni/Fe and Ni/Cr molar ratios equal to 2 and 3. Finally, the Ni-Fe and Ni-Cr mixed oxides were tested in the CO_2 reforming of methane at low reaction temperatures (400–650 °C). The influences of the molar ratio and the cationic composition in the preparation of the LDH precursors on the physicochemical properties of the target catalysts and on their performance in DRM were evaluated. A set of characterizations before (LDH) and after (LDO) thermal treatment at 500 °C using TGA-TD-SM, HT-XRD, XRD, Raman, and IR-ATR spectroscopies; N_2 physical adsorption; XPS; and H_2-TPR were also performed to attain structure–reactivity relationships and enhance hydrogen production.

2. Results

2.1. Structural Characterization (XRD, Raman, and FTIR) of LDH Precursors

The XRD patterns recorded at room temperature for LDH precursors (Figure 1) show the presence of Bragg reflections located at 2θ values of 11.27°, 22.79°, 33.8°, 38.6° and 60.6°, related to the (003), (006), (012), (015), and (110) crystallographic planes of LDH phase with rhombohedral symmetry (R3), in accordance with previous works [15]. The d-spacing values calculated from the position of (003) diffraction lines of Ni_2Cr, Ni_3Cr, Ni_2Fe, and Ni_3Fe-LDH are about 7.82 Å, 7.77 Å, 7.94 Å, and 7.94 Å, respectively. These values were ascribed to CO_3^{2-} anions and water molecules intercalation in the LDH interlayer space, and hence the synthesis was performed an ambient atmosphere. Additionally, the relative

weak intensities and wider peaks of (00l) diffractions suggest a low crystallinity of the as-prepared LDHs [16]. The lattice parameters "*a*" and "*c*" calculated for the four precursors are gathered in Table 1. The values are in good agreement with the literature; that is, the "*c*" and "*a*" values decrease with lower Ni/Cr and Ni/Fe molar ratios.
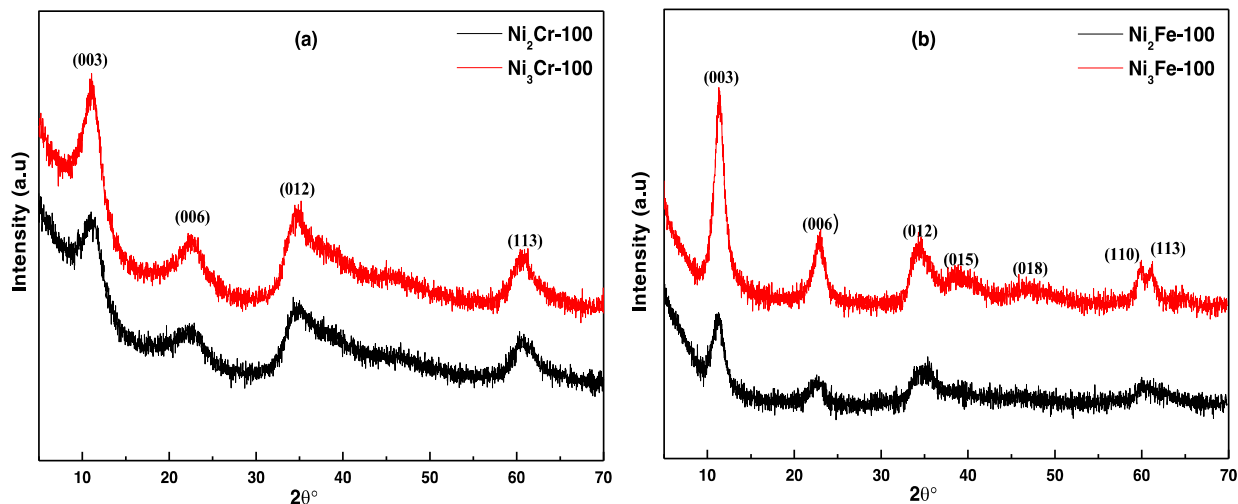

Figure 1. XRD patterns of Ni_RCr (**a**) and Ni_RFe (**b**) LDH precursors.

Table 1. Structural parameters of Ni_RFe and Ni_RCr LDH precursors obtained from XRD patterns.

LDH	d_{003} (Å)	d_{110} (Å)	a (Å) [1]	c (Å) [1]
Ni_2Fe	7.82	1.53	3.06	23.46
Ni_3Fe	7.77	1.54	3.08	23.31
Ni_2Cr	7.94	1.52	3.04	23.82
Ni_3Cr	7.94	1.53	3.06	23.83

[1] Lattices parameters a and c are equal to $2 \times d_{(110)}$ and $3 \times d_{(003)}$, respectively.

Figure 2 shows the Raman spectra of the precursors Ni_RFe LDH and Ni_RCr LDH (R = 2, 3) in the relevant spectral range to study hydrotalcites (300–1200 cm^{-1}), the water molecule is better detected by infrared absorption than by Raman scattering. The line observed at 1049 cm^{-1} accompanied by its shoulder at 1069 cm^{-1} is attributable to the elongation vibration of the carbon–oxygen bond of the CO_3^{2-} group in agreement with the work of Frost et al. [17].
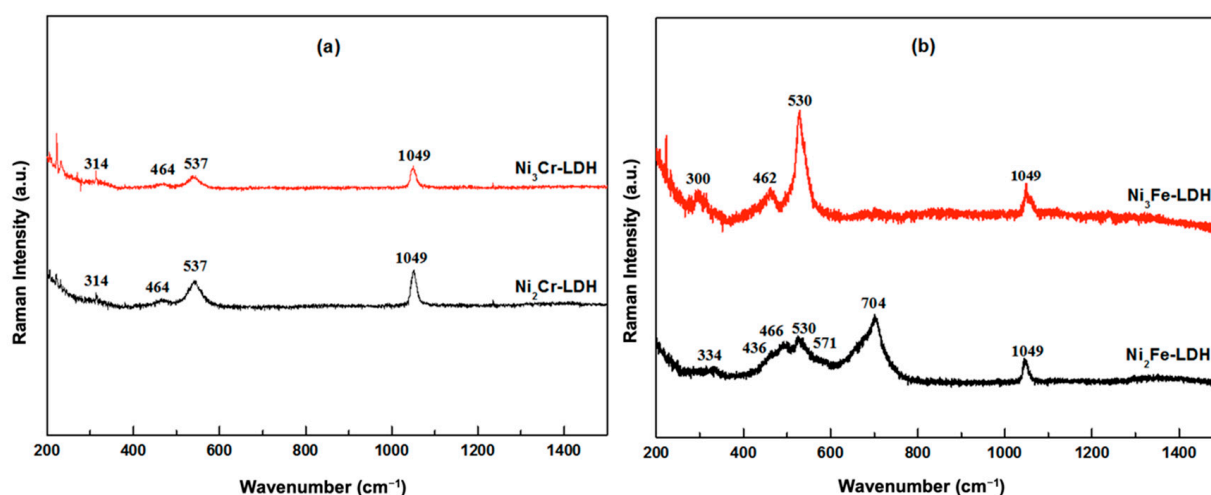

Figure 2. Raman spectra of Ni_RCr (**a**) and Ni_RFe (**b**) LDH precursors.

Comparing with the value of 1080 cm^{-1} generally obtained for pure carbonates [18], the band shift towards the low frequencies reveals interactions with the carbonate ion in the layers, with the shoulder indicating a slightly different environment for oxygen of this ion.

The Raman spectra of the Ni$_2$Fe and Ni$_3$Fe LDH precursors have different spectral features (Figure 2b). For the first, the observation of bands at 704, 571, 436, and 334 cm^{-1} wave numbers, indicates a strong dominance of the NiFe$_2$O$_4$ reverse spinel [19]. This strong presence is not found for Ni$_3$Fe LDH for which it is difficult to observe the most intense band of the NiFe$_2$O$_4$ spectrum at about 700 cm^{-1}, representative of the symmetrical elongation mode of the tetrahedral entity [FeO$_4$] composing the inverse spinel with the octahedral [FeO$_6$] and whose vibration modes are located in the spectral range of 300–600 cm^{-1} [20]. Nevertheless, for this spectral domain, three bands are recorded at 530, 462, and 300 cm^{-1}. The most intense one at 530 cm^{-1} for Ni$_3$Fe LDH, also observable for Ni$_2$Fe LDH, and with the broad band at 462 cm^{-1} constitute a doublet attributable to the Ni(OH)$_2$ species, according to the reference [21], which is in agreement with the presence of hydroxyl ions in the layers. The weak band at 300 cm^{-1} could be due to Fe$_2$O$_3$ [22].

The spectral features of the Ni$_2$Cr and Ni$_3$Cr LDH precursors are similar (Figure 2a). The bands with weaker intensity are comparable to the 1049 cm^{-1} intensity line assigned to the carbonate ion in the layers. The most intense and characteristic line of the tetrahedron [CrO$_4$], located in the spectral range 800–900 cm^{-1}, are not detected on these precursors. The band observed at 537 cm^{-1}, one of the most intense in the spectrum, is attributable to chromium oxide Cr$_2$O$_3$, according to the work of J. Singh et al. [23]. The band width can be due to an overlap with the characteristic line of Ni(OH)$_2$.

Figure 3 shows the IR-ATR absorption spectra of these different precursors for which the spectral feature is quite similar, except in the 400–1000 cm^{-1} domain. The wave numbers recorded at 3400 cm^{-1} for symmetrical elongation of the bond νs (O-H) and at 1630 cm^{-1} for angular deformation δs (H$_2$O) clearly indicate the formation of hydrogen bonds in the hydrotalcite layers and in particular with carbonate ions whose unsymmetrical elongation frequency ν_d (C=O) shifts towards the low wavenumbers 1351 cm^{-1} [24]. This is in agreement with the results obtained by Raman scattering for the symmetrical elongation frequency νs (C=O) observed at 1049 cm^{-1}.
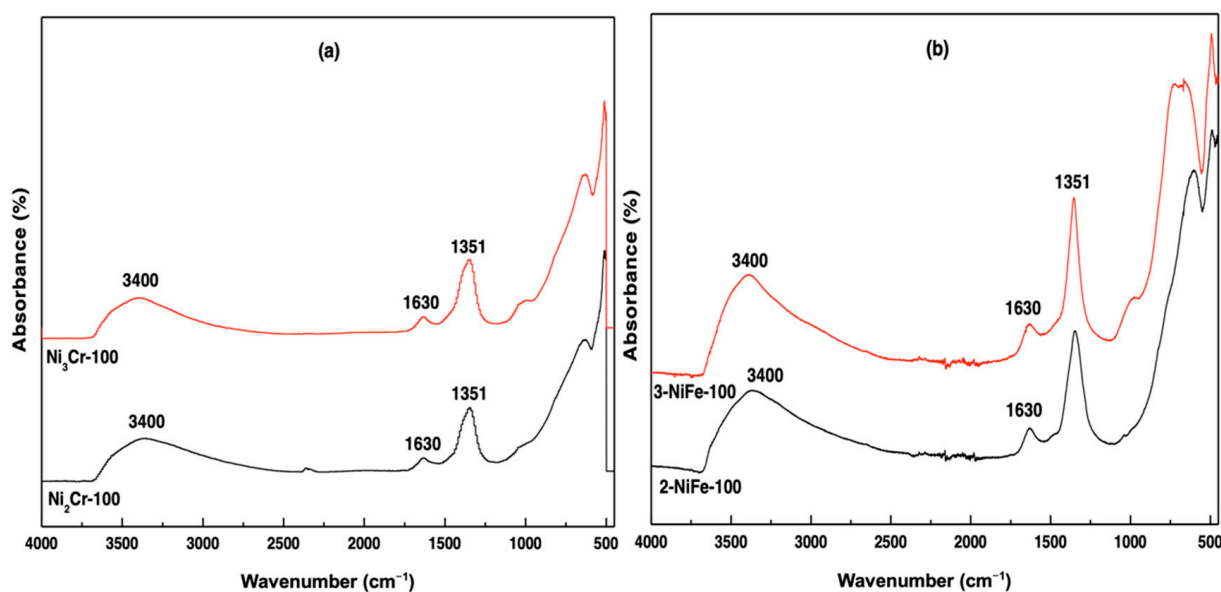

Figure 3. IR-ATR spectra of Ni$_R$Cr (**a**) and Ni$_R$Fe (**b**) LDH precursors.

2.2. Thermal Decomposition (HT-XRD and TG-DTA) of LDH Precursors

The recorded TG-DTA thermograms when Ni$_R$Fe and Ni$_R$Cr LDH were subjected to thermal decomposition are shown in Figure 4.
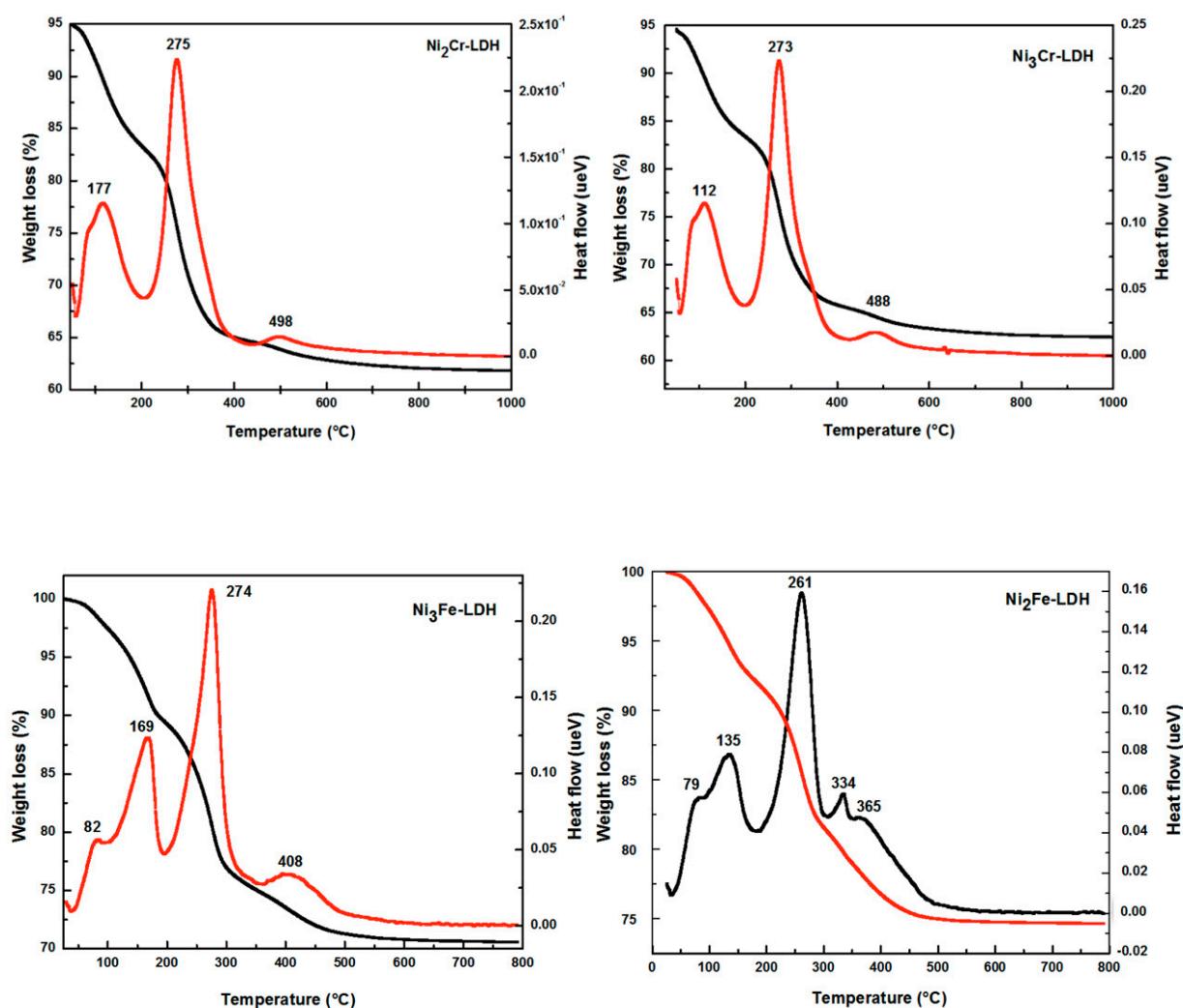
Figure 4. TG-DTA curves of Ni_RCr and Ni_RFe LDH precursors.

The thermal behavior analysis indicates mainly three steps of weight loss up to $\approx600\ ^\circ C$ for Ni_RCr and Ni_RFe LDH. There is no weight loss or heat flow observed above $600\ ^\circ C$. This implies that there is no phase change above $500\ ^\circ C$. The total weight loss is higher in the Ni_RCr LDH case ($\approx32\%$) compared to Ni_RFe LDH (≈24 and $\approx27\%$ for Ni_2Fe and Ni_3Fe, respectively).

The species responsible for the weight loss are water, carbonates, and nitrates. Through online mass spectroscopy (MS), m/z = 18, 30, 44, and 46, corresponding to H_2O, NO, CO_2 and NO_2, respectively, were followed and are reported in Figures S1 and S2 and summarized in Table S1. During the three steps, the release of H_2O was observed in the first and second stages, while NO, NO_2 and CO_2 occurred in the second and third steps. During the first step from ambient to $200\ ^\circ C$, MS analysis showed that only the removal of water physically adsorbed on the external surface of the crystallites and interlayer spaces with a weight loss of ~12% for Ni_RCr and ~8–10% for Ni_RFe. In the two other stages ($200{\to}320\ ^\circ C$ and $320{\to}600\ ^\circ C$), the release of H_2O is also observed and is accompanied by the departure of carbonates and nitrates from the LDH structure. Both steps correspond to the concurrent dehydroxylation of the brucite-like layers and the decomposition of the intercalated anions [25]. As the temperature further increases, the weights of the samples remain constant, with no obvious endothermic/exothermic peak, indicating that the structure of the materials reaches relative stability. The theoretical weight loss for the transformation of $Ni(OH)_2$, $Cr(OH)_3$ and $Fe(OH)_3$ hydroxides to Ni-Cr-O and to Ni-Fe-O

oxides is $\Delta m/m$ = 23–25%. This value was approximately reached in the Ni_RFe samples, but a slight difference was observed for Ni_RCr LDH formulations (Table S1).

The transformation of Ni-Fe-LDH precursors was studied by HT-XRD up to 800 °C in air (Figure 5). The hydrotalcite structure is observed at room temperature and up to 250 °C. At 275 °C, it fully collapsed into oxide (Layer Double Oxide-LDO) due to the dehydroxylation of the layer and removal of NO_x and CO_2 from the interlayer, as observed at a similar temperature in TGA analysis (Figure 4). Until 800 °C, only the lines of the NiO (PDF: 01-080-5508) phase are observed and become sharper and more symmetric with increasing temperature. No other crystalline structure was detected, showing that Fe(III) is dispersed in the NiO rock salt phase as a solid solution.
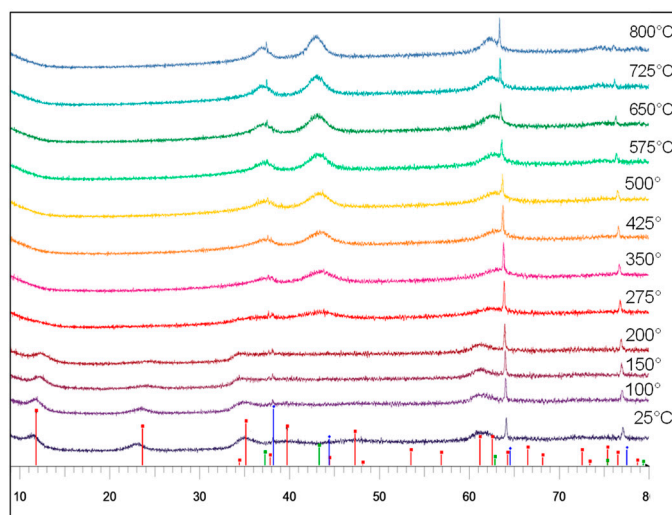

Figure 5. HT-XRD patterns of Ni_3Fe LDH precursor decomposition in air.

Lattice parameters *a* and *c* and interlayer space (d_{003}) were calculated as a function of temperature and are listed in Table 2. During HT-XRD measurements, from 25 to 250 °C, the values of the lattice parameter (*a*) are similar. However, the values of lattice parameter (*c*) and interlayer space (d_{003}) decrease markedly when the temperature increases as a result of a dehydration phenomenon and a strengthening of the interaction between interlayer anions and hydroxide layers during heating treatment. Benito et al. [26] and Kovanda et al. [27] reported the same observations concerning the change in lattice parameter (*c*) and interlayer space (d_{003}). Further heating of the powder induces a decrease in the intensity of LDH structure lines, which disappear completely at 275 °C (Figure 5). This result is in agreement with those obtained from TGA analysis. The temperature of decomposition is higher in TGA due to a different heating rate which yields different kinetics.

Table 2. Evolution of lattice parameters of Ni_3Fe-LDH as a function of temperature.

Temperature (°C)	d_{003} (Å)	*a* (Å) [1]	*c* (Å) [1]
25	7.814	3.010	23.442
50	7.694	3.015	23.082
75	7.665	3.027	22.995
100	7.576	3.027	22.728
125	7.467	3.023	22.401
150	7.399	3.027	22.197
175	7.265	3.012	21.795
200	7.221	3.015	21.663
225	7.102	3.015	21.306
250	7.017	3.018	21.051

[1] Lattices parameters *a* and *c* are equal to $2 \times d_{(110)}$ and $3 \times d_{(003)}$, respectively.

2.3. Characterization (XRD, Raman, BET, XPS, and H₂-TPR) of Mixed Oxide Catalysts

X-Ray Diffraction and Laser Raman spectroscopy analyses were used to ascertain the structural properties of catalysts obtained after calcination at 500 °C. The LDH structure is fully destroyed due to the elimination of most interlayer anions (NO_x and CO_x) and water. As highlighted by TGA and HT-XRD analysis, LDH decomposition leads to mixed metal oxide structures.

As can be seen in Figure 6a, XRD patterns of Ni_2Cr-500 and Ni_3Cr-500 show similar diffractograms. Ni/Cr ratio used in the preparation has little effect on the structures of the resulting materials. The diffractograms (Figure 6a) confirm the presence of NiO and $NiCr_2O_4$ structures, where peak positions of $2\theta \approx 37.4, 43.3, 62.9$, and $75.5°$ correspond to the (111), (200), (220), and (311) family of planes of NiO structure (PDF: 03-065-2901), while the characteristic diffraction peaks at $18.4°, 30.3°, 35.8°$, and $57.4°$ belongs to the (111), (220), (311), and (511) planes of $NiCr_2O_4$ in accordance with PDF 85-0935. In contrast, for Ni_2Fe-500 and Ni_3Fe-500 samples, different diffractograms were obtained (Figure 6b), suggesting that the amount of Ni species used has a significant effect on the crystalline structure of Ni_RFe-500 catalysts. For the low amount of Ni-species (R = 2), a mixture of phases was detected containing NiO (PDF: 03-065-2901) ($2\theta \approx 37.4$ (111), 43.3 (200), 62.9 (220), and 75.5° (311)) and $NiFe_2O_4$ (PDF: 00-054-0964) spinel structure by the peaks located at ≈ 18.4 (111), 30.3 (220), 35.8 (311,) and 57.4° (511). However, the sample Ni_3Fe-500 matches only the NiO oxide phase (PDF: 03-065-2901) through the reflections located at $2\theta \sim 37.5, 43.6$ and $75.5°$. The possibility of $NiFe_2O_4$ spinel oxide formation in Ni_3Fe-500 formulation cannot be excluded as it could be present in a very low amount or well-dispersed form which would make it difficult to be detected by the XRD.
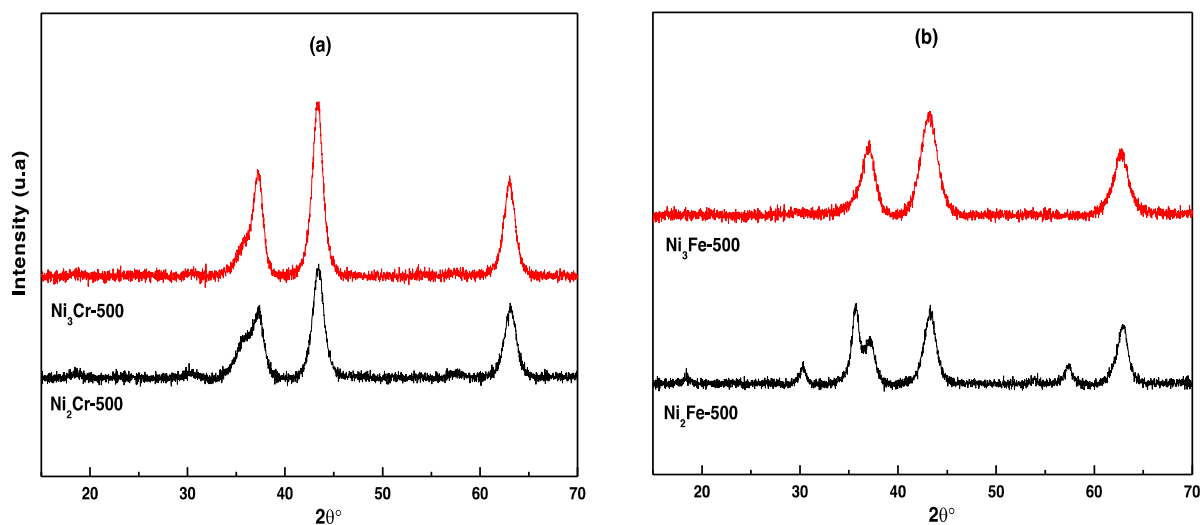

Figure 6. XRD patterns of Ni_RCr-500 (**a**) and Ni_RFe-500 (**b**) catalysts.

No characteristic peak corresponding to Cr_2O_3 and Fe_2O_3 phases could be detected for Ni_RCr-500 and Ni_RFe-500, respectively, which is probably due to their low crystallinity. In all cases, we observed NiO oxide as the dominant phase. No obvious diffraction peaks of the spinel phase were observed, which, considering the calcination temperature and the relatively low Fe and Cr loadings, may be related to the formation of amorphous or well-dispersed phases, not detected by X-ray diffraction.

The crystallite size (CS) for all samples has been calculated using XRD data and are reported in Table 3. Both samples, Ni_2Cr-500 and Ni_3Cr-500, which show the same crystalline structure (Figure 6a), exhibit similar crystallite size values (75–77 Å). In contrast, Ni_2Fe-500 and Ni_3Fe-500 samples show different crystallite sizes (69 Å for Ni_2Fe-500 against 53 Å for Ni_3Fe-500) suggesting an effect of the amount of Ni-species incorporated in the LDH structure.

Table 3. Textural properties of Ni-based catalysts.

Catalysts	Cs [1] (Å)	S_{BET} (m² g⁻¹)	Pore Volume (cm³ g⁻¹)	Mean Pore Diameter (Å)	
				B.E.T.	B.J.H.
Ni₂Fe-500	69	144	0.24	76	62
Ni₃Fe-500	53	160	0.39	91	76
Ni₂Cr-500	75	73	0.18	92	79
Ni₃Cr-500	77	74	0.23	124	107

[1] Crystallites size of NiO phase, BET surface area, pore volume, and pore diameter. The pore diameter parameter was obtained from BET and BJH methods.

Figure 7 shows the Raman spectra of the catalysts Ni_RFe-500 and Ni_RCr-500 (R = 2, 3) after calcination at 500 °C. In comparison with Figure 2b, one can note the disappearance of the bands located at 300, 462, and 530 cm⁻¹, accompanied by the reinforcement of the band intensity at 578 cm⁻¹. This indicates the transformation of $Ni(OH)_2$ into NiO [21]. For the Ni_2Fe-500 catalyst, a high proportion of $NiFe_2O_4$ in the mixture can be noted.
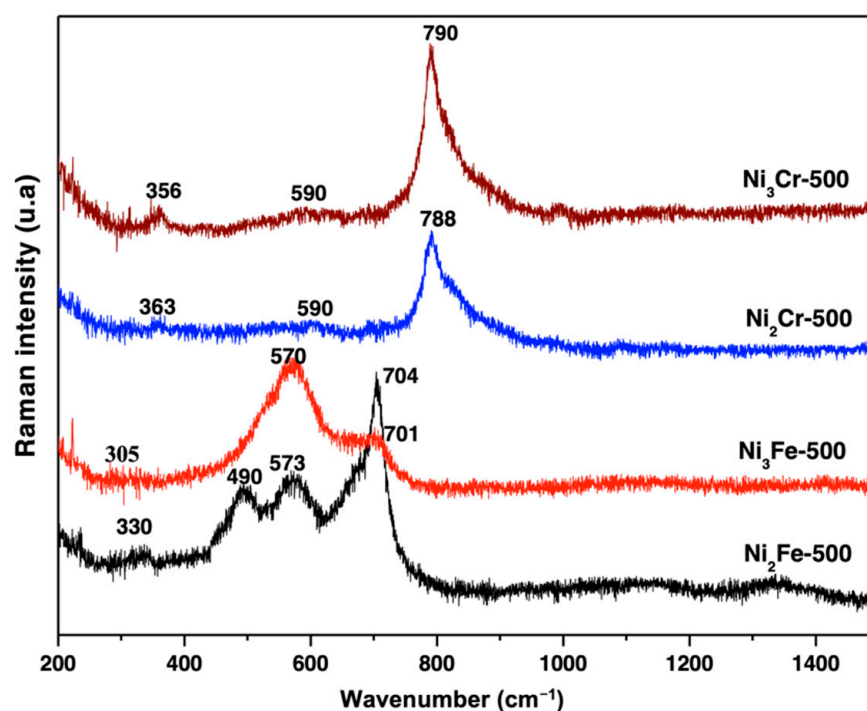
Figure 7. Raman spectra of Ni_RCr-500 and Ni_RFe-500.

The spectral feature (wide band) associated with the wavenumber values (707, 570 and ~305 cm⁻¹) for Ni_3Fe-500 suggests the coexistence of $NiFe_2O_4$ and $FeFe_2O_4$ spinels [28,29] with NiO nickel oxide.

For the Ni_RCr-500 samples, the spectra (Figure 7) show an intense and asymmetrical band, whose maximum is recorded at 791 cm⁻¹. It characterizes the symmetrical elongation movement of the tetrahedron [CrO₄]. The anti-symmetrical elongation vibrations of this same entity are represented by the different components forming the asymmetry of this band. The other modes of angular deformation of the tetrahedron, of lower intensity, are embedded in the wide and low band centered on 590 cm⁻¹. These results are in good agreement with the work of D'Ippolito et al. [30].

The textural properties of the catalysts after calcination at 500 °C were determined from the nitrogen adsorption–desorption isotherms at 77 K. The specific surface area values measured by BET are reported in Table 3. The N₂ adsorption–desorption isotherms of catalysts (Figure 8) are type IV according to IUPAC classification with H3-type hysteresis

loop, indicating mesoporous materials. Furthermore, the hysteresis shape suggests slit-type pores with a void created by particle aggregation and attributed to open pores at both ends [31,32].
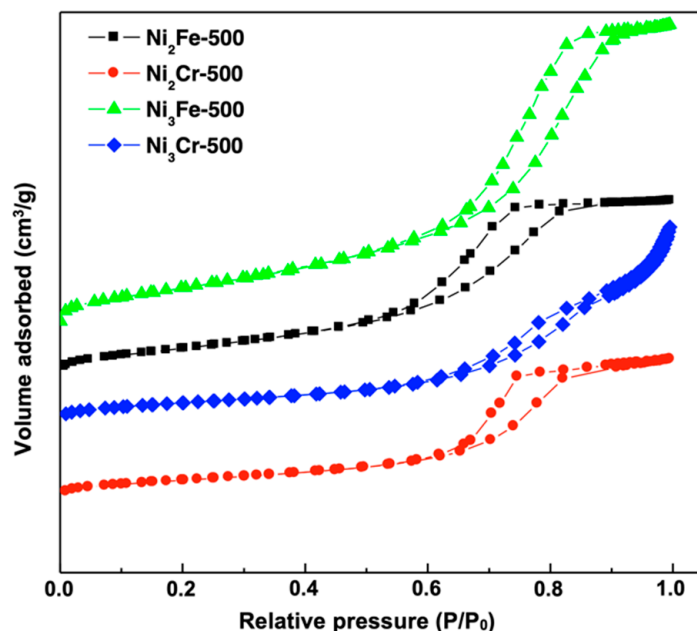

Figure 8. N_2 adsorption–desorption isotherms of Ni_RCr-500 and Ni_RFe-500 catalysts.

As can be seen in Table 3, the textural parameters of the solids follow the same trend; i.e., the values of BET surface area, pore volume, and pore diameter show a progressive increase with increasing Ni to trivalent metal ratios. The specific surface areas of Ni_RFe are approximately two times greater than that of Ni_RCr. The highest specific surface area value of Ni_3Fe catalyst (160 m^2/g) is in accordance with the smallest respective crystallite size (53 Å, Table 3).

Chemical state and surface compositions of the catalysts were examined by XPS analysis. Figures S3–S6 (see SI) represent the photoemission spectra of *2p* levels of nickel (*Ni2p3/2* line), *2p* of iron (*Fe2p3/2* line), *2p* of chromium (line *Cr2p3/2*), and *1s* of oxygen (*O1s* line) obtained on the various samples calcined at 500 °C. The values of the binding energies of *Ni2p3/2*, *Fe2p3/2*, *Cr2p3/2*, and *O1s* lines, as well as the results of the quantification of the atomic ratios Ni/Fe and Ni/Cr, calculated from the photopeak intensities are gathered in Table 4.

Table 4. Binding energy (eV) and Ni/M atomic ratios (M = Fe or Cr) obtained by XPS.

Catalysts	Binding Energy (eV)			Atomic Ratio [1]	
	Ni	Fe	Cr	Ni/Fe	Ni/Cr
Ni_2Fe-500	854.7	711.1	-	0.7	-
Ni_3Fe-500	854.9	711.6	-	0.9	-
Ni_2Cr-500	855.0	-	576.5	-	2.2
Ni_3Cr-500	855.0	-	576.9	-	3.2

[1] Atomic ratio equal to 2 or 3.

The surface compositions depend on the nature of the used metals. Both chromium-based catalysts (Ni_2Cr-500 and Ni_3Cr-500) show Ni/Cr ratio very close to the nominal bulk composition, suggesting little or negligible surface segregation on these samples. In contrast, Ni_2Fe-500 and Ni_3Fe-500 catalysts show a Ni/Fe atomic ratio lower than expected, highlighting the presence of more iron species on the surface than in the bulk of the catalysts. This excess in iron species on the surface can be correlated to the nature of $NiFe_2O_4$ inverse

spinel structure as Fe(III+) species occupy both crystallographic positions: 50% of the ions in the octahedral-[Oh] position and 50% in tetrahedral-[Td] sites.

The decomposition of the spectra for Ni, Cr and O species shows two components, while only one component is observed for Fe (Figures S3–S6). For the latter, the binding energy values are 711.1 eV for Ni_2Fe-500 and 711.6 eV for Ni_3Fe-500 (Figure S3), accompanied by the presence of a satellite peak at higher energy (7.7 eV) vs. the main peak as a clear indication of the presence of Fe(III) species only on the catalyst surface [33]. The *Ni2p3/2* peaks (Figure S4), are composed of the main peak located at ≈855 eV and a relatively intense satellite peak at about 7 eV higher energy. The existence of such a satellite is characteristic of the oxidation state (+II) of nickel [33,34]. According to literature data [31,32], the decomposition of these spectra (Figure S4) shows the presence of Ni (II+) in NiO by the lines located at ≈855. $Ni(OH)_2$ hydroxide (Ni, II+) shows values close to that of NiO oxide (861 and 867 eV), but its presence can be excluded because the calcination is carried out at 500 °C where the total transformation of $Ni(OH)_2$ hydroxide into oxide is ensured. The peaks situated at ≈856 and 862 eV can therefore be attributed to nickel in the spinel structure (Ni in $NiFe_2O_4$ or in $NiCr_2O_4$). Both Ni_2Cr-500 and Ni_3Cr-500 systems show similar *Cr2p* spectra (Figure S5). The binding energy value of the *Cr2p* line is 576.5 and 576.9 eV for Ni_2Cr-500 and Ni_3Cr-500, respectively. These values characterize the presence of Cr^{3+} in our formulations. After the decomposition of the spectra (Figure S5) of *Cr2p*, we note the appearance of a band around 579.1 eV for Ni_2Cr-500 and 579.3 eV for Ni_3Cr-500 which can be associated with Cr^{6+} species [33]. Several studies reported that a fraction of Cr^{3+} ions exposed in the chromium oxide is easily oxidized to Cr^{6+} during the calcination step under an ambient atmosphere [35]. The photopeak *1s* of oxygen (Figure S6) reveals two components for all formulations. The first component, corresponding to the lowest binding energy (~530 eV), is associated with the lattice oxygen O^{2-} and the second component of higher binding energy (~ 532 eV), is due to the presence oxygen localized on the outer layer of the solid and belonging to -OH groups or probably to H_2O adsorbed on the surface.

The H_2-TPR profiles are given in Figure 9. The hydrogen consumption displays different profiles depending on both the trivalent cation and the molar ratios used. The amount of consumed H_2 depends significantly on the nature of the trivalent metal (Fe or Cr) and does not depend on the Ni/M ratios (M = Fe, Cr); the amount of consumed H_2 for Ni_RFe-500 (16–17 mmol/g) catalysts is greater with a factor of ≈2 compared to that of Ni_RCr-500 (9–10 mmol/g).
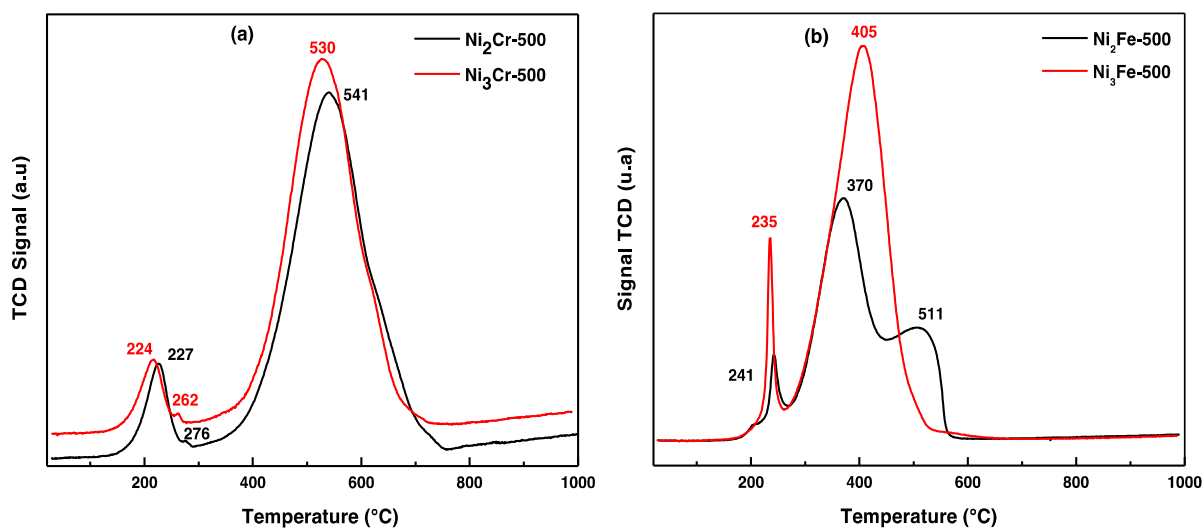

Figure 9. H_2-TPR profiles of Ni_RCr-500 (**a**) and Ni_RFe-500 (**b**).

The Ni$_2$Cr-500 and Ni$_3$Cr-500 catalysts possess a similar TPR with reduction peaks, which shift slightly to higher temperature upon decreasing Ni/Cr ratio. This means that the Ni$_2$Cr-500 catalyst is less reducible and more stable. In Figure 9a, two domains of hydrogen consumption can be observed in the temperature region 200–700 °C, which are related mainly to the reduction of both Ni^{2+} species. For both chromium-based catalysts, the first peak of H$_2$ consumption at 227 for Ni$_2$Cr-500 and at 224 °C for Ni$_3$Cr-500 is correlated to the reduction of surface oxygen species, which can be reduced by hydrogen at low temperatures [36]. The peaks at about 262–276 °C and at 530–541 °C could be attributed to the reduction of Ni^{2+} present in NiO and in the lattice of NiCr$_2$O$_4$ spinel phase detected by XRD and Raman analyses as mentioned above.

In contrast to Cr-based catalysts, the H$_2$-TPR of iron-based catalyst exhibits two different profiles (Figure 9b) according to the Ni/Fe ratio. Ni$_2$Fe-500 catalyst exhibits three reduction peaks centered at 241, 370, and 511 °C. The first and the second peaks (located at 241 and 370 °C) may be attributed to the simultaneous reduction of (i) Ni(II+) present in NiO and in NiFe$_2$O$_4$ and (ii) Fe(III+) in tetrahedral-[Td] sites of the NiFe$_2$O$_4$ spinel phase. The third peak located at 511 °C is assigned to the reduction of Fe^{3+} in the octahedral-[Oh] position of the NiFe$_2$O$_4$ structure. However, the catalyst richer in Ni species (Ni$_3$Fe-500) shows a fairly similar profile compared to NiO oxide [37] in accordance with XRD data, which showed only NiO oxide (Figure 6). The profile reveals two neat reduction peaks centered at 225 and 405 °C. The first of low intensity at ~225 °C and the second with strong intensity at ~405 °C are attributed to the reduction of amorphous α-NiO and clustered β-NiO, respectively.

2.4. Catalytic Properties in CO$_2$-Reforming of Methane

The catalysts obtained after synthesis (LDH) and calcination at 500 °C under air flow (LDO) were tested for DRM. Figures 10 and 11 and Table S2 show the catalytic performances (CH$_4$ conversion and CO$_2$ conversion, H$_2$ selectivity and H$_2$/CO ratio) obtained in temperature-programmed reaction conditions between 400 and 650 °C.
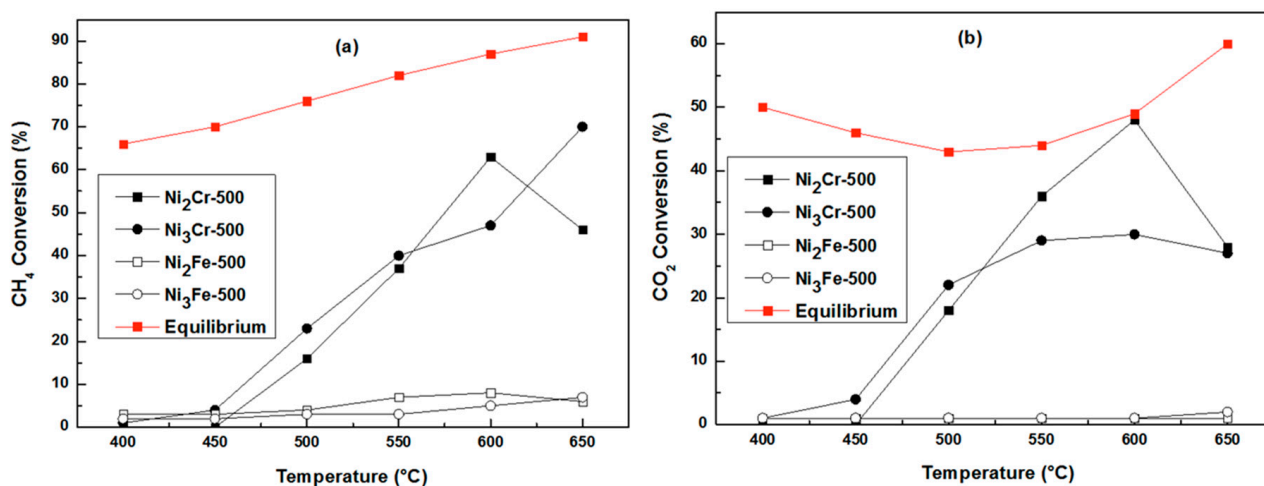

Figure 10. CH$_4$ (**a**) and CO$_2$ (**b**) conversions obtained on the fresh Ni$_R$M-500 (M = Cr or Fe, R = 2 or 3) catalysts issued from LDH structure and calcined at 500 °C (CH$_4$ = 20%; CO$_2$ = 20%; 100 mg; F = 100 mL/min).

Both chromium-based catalysts (Ni$_2$Cr-500 and Ni$_3$Cr-500) are catalytically active and selective. The conversions of CH$_4$ and CO$_2$ (Figure 10), H$_2$-selectivity, and H$_2$/CO ratio (Figure 11) show very similar behaviors, suggesting the little effect of Ni/Cr ratios on the catalytic performances for these formulations.
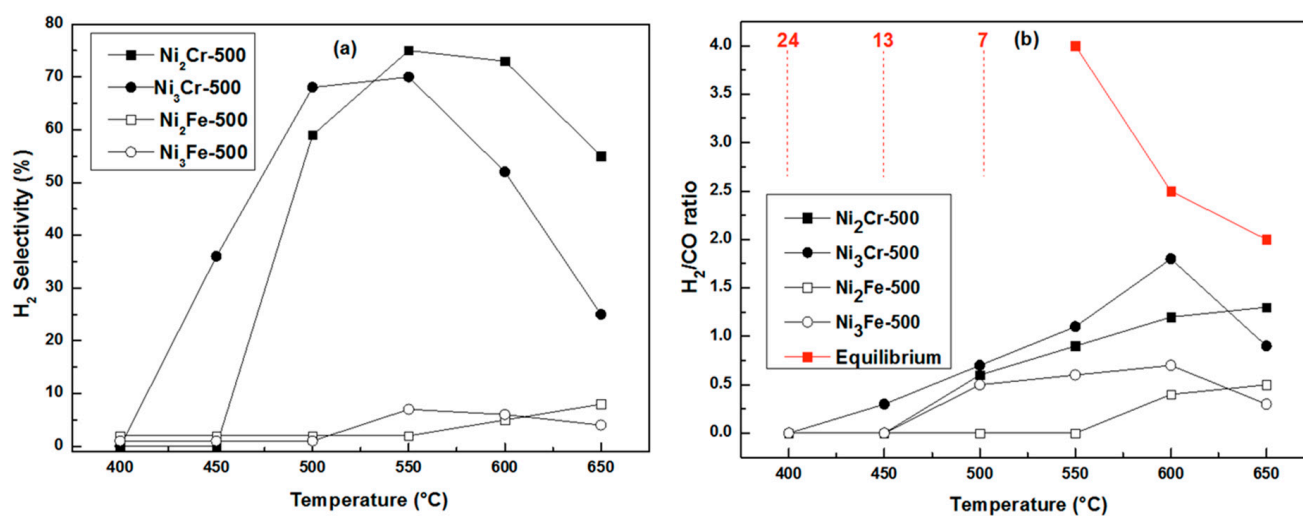
Figure 11. H_2 selectivity (**a**) and H_2/CO ratios (**b**) obtained on the fresh Ni_RM-500 (M = Cr or Fe, R = 2 or 3) catalysts issued from LDH structure and calcined at 500 °C (CH_4 = 20%; CO_2 = 20%; 100 mg; F = 100 mL/min).

This behavior is not very surprising because both systems, as shown in the characterization section, have similar structural (NiO and $NiCr_2O_4$ in their structure) and textural (73–74 m^2/g and Ni/Cr ≈ stoichiometry) properties. CH_4 and CO_2 conversion remain well below equilibrium values in the full range of temperature explored. In particular, in the 450–550 °C range, thermodynamics should favor CH_4 conversion and carbon deposition on one side, and CO_2 conversion through RWGS to form water on the other. This would lead to significantly higher methane conversion with respect to CO_2 conversion, strong carbon deposition, and a high H_2/CO ratio (above 4). The performances observed for Ni_2Cr-500 and Ni_3Cr-500 samples are very far from the thermodynamic conversions, confirming that the reactivity is effectively governed by the catalytic properties of the materials.

Moreover, if one looks more carefully at the values obtained at 500 °C (Table 5), both chromium-based samples show rather similar behaviors. Conversions of methane are in the range of 16–23% for the two samples and are close to those of CO_2. Hydrogen selectivity is high (60–70%), whereas H_2/CO is around 0.7. Water is certainly produced, either through a contribution of RWGS reaction or through the reduction of the solid. These results remain exceptional in terms of selectivity in such low temperature ranges.

Table 5. DRM performances at 500 °C in temperature-programmed and isothermal modes.

Catalysts	X% CH_4	X% CO_2	S% H_2	H_2/CO
Ni_2Cr-500 (TP [1])	16	18	59	0.6
Ni_3Cr-500 (TP [1])	23	22	68	0.7
Ni_2Fe-500 (TP [1])	4	1	2	-
Ni_3Fe-500 (TP [1])	3	1	1	0.5
Ni_2Cr-500 (ISO [2], t = 20 min)	30	18	40	1
Ni_3Cr-500 (ISO [2], t = 20 min)	16	21	88	0.7

[1] TP: temperature programmed mode (cf. Figures 10 and 11); [2] ISO: isothermal mode (cf. Figure 12).

Above 600 °C, the curves of CH_4 and CO_2 conversion do not increase anymore as should be expected. On the contrary, the catalysts are progressively deactivated. This catalytic behavior is very different from the results obtained in our previous work [36] on Ni-Cr spinel oxide prepared by the coprecipitation method. These catalysts showed excellent activity both in terms of conversions and selectivity at a high temperature, whereas below 700 °C, carbon deposition mostly occurred even though the Ni content of those catalysts was much lower (Ni/Cr = 0.5 as compared to 2 or 3 in the present catalysts). The carbon

deposition is usually attributed to large metallic nickel particles. The results obtained at a low temperature on Ni$_2$Cr-500 and Ni$_3$Cr-500 are therefore particularly interesting.
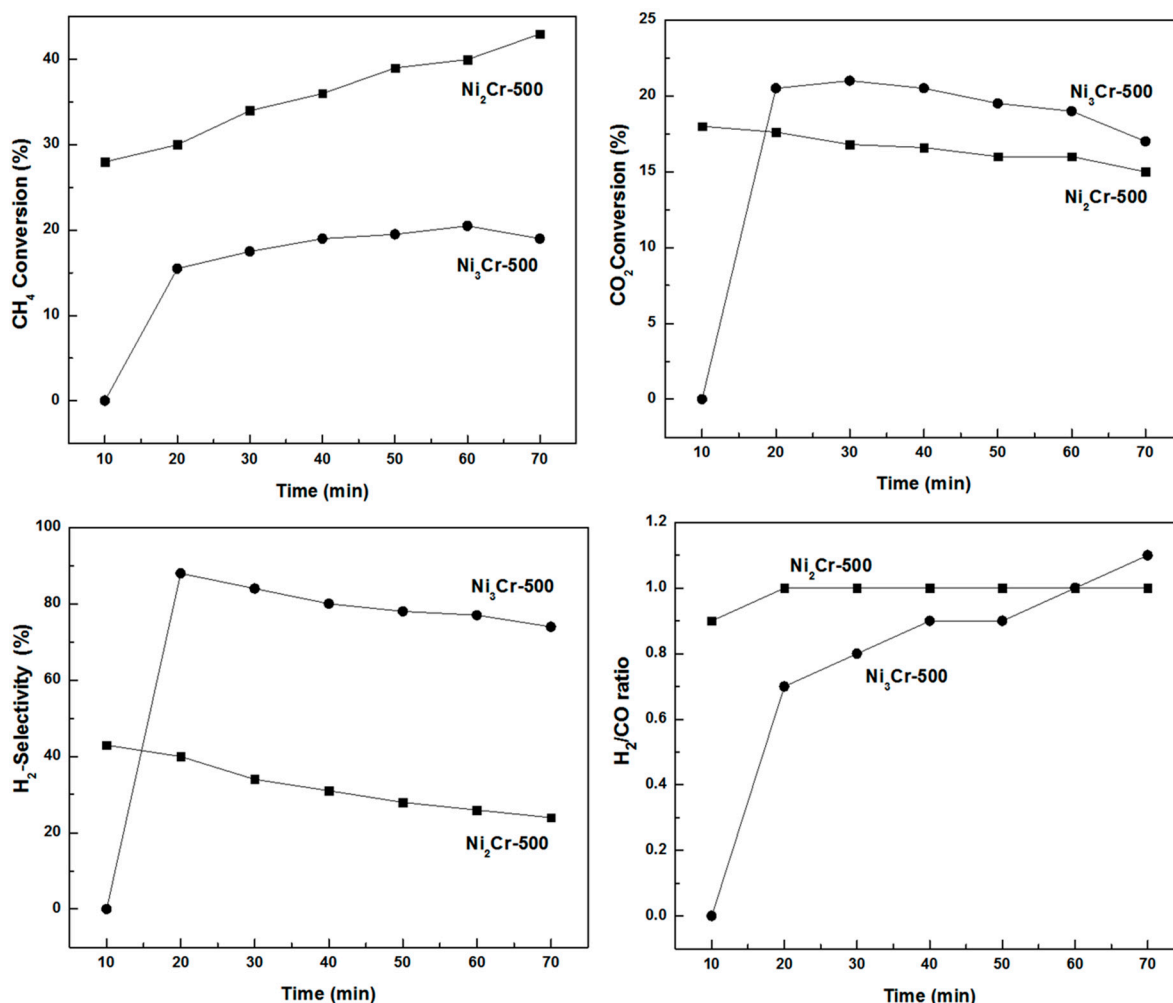

Figure 12. Isothermal test of catalytic performances in terms of conversions (CH$_4$ and CO$_2$), H$_2$ selectivity and H$_2$/CO of fresh Ni$_2$Cr-500 and Ni$_3$Cr-500 catalyst at 500 °C. (CH$_4$ = 20%; CO$_2$ = 20%; 100 mg; F = 100 mL/min).

For Ni$_2$Fe-500 and Ni$_3$Fe-500, a very different catalytic behavior from those of Ni$_R$Cr-500 was noticed. In spite of their high specific surface area (144–160 m^2/g, Table 3) and their low crystallite size (53–69 Å), both samples showed poor catalytic performances at all temperatures in the range of 400–650 °C (Figures 10 and 11). In addition, although Ni$_2$Fe-500 and Ni$_3$Fe-500 samples have different reducibility patterns (Figure 9), the activity remains almost negligible for both catalysts. The low activity of Ni$_2$Fe-500 and Ni$_3$Fe-500 is rather surprising because the amount of Ni species used in departure, which is responsible for DRM reaction, is the major constituent of the catalysts with respect to iron (Ni/Fe = 2 or 3). However, the catalytic behavior of Ni$_2$Fe-500 and Ni$_3$Fe-500 obtained from LDH structure is similar to ferrite spinel nanoparticles prepared by coprecipitation [19], hydrothermal [19] and sol-gel [38] methods. We can assign the poor catalytic performances of Ni$_R$Fe-500 to the presence of excess Fe^{3+} species on the Ni$_R$Fe-500 surface as revealed by XPS (Table 4). The Fe^{3+} species mainly favor RWGS reaction. On the other hand, the low activity can be linked to the disappearance of active Ni-metallic phase related to the formation of Ni-Fe alloy at the expense of Ni° and Fe° reduced species under reaction mixture, as confirmed in our previous works by in situ HT-XRD under flowing H$_2$ [19,38].

To better evaluate the catalytic properties of Ni_2Cr-500 and Ni_3Cr-500 catalysts, the fresh catalysts were heated from RT to reaction temperature in inert gas and then exposed to DRM mixture at 500 °C. Figure 12 shows the evolution of CH_4, CO_2 conversions, H_2 selectivity, and H_2/CO as a function of time. Ni_2Cr-500 shows higher conversion than Ni_3Cr-500, but activity decreases progressively with time, whereas that of Ni_3Cr-500 remains rather stable throughout the period studied (up to 70 min). CO_2 conversions are in the same range and tend to diminish with time on both samples. Although methane conversion increases and CO_2 decreases, the H_2 selectivity tends to decrease with time, while H_2/CO is very stable (Ni_2Cr-500) or increases progressively (Ni_3Cr-500) tending to the optimal stoichiometry of $H_2/CO = 1$. This is rather surprising, especially on Ni_2Cr-500, given that CO_2 conversion is significantly lower than that of CH_4 on this catalyst. This suggests that the presence of Cr^{3+} species probably limits CO_2 activation and the participation of sides reactions such as RWGS. However, in such conditions, higher H_2 selectivity and H_2/CO ratio should be expected. The low values observed can only be explained by simultaneous water production (not quantified), which would need a significant supply of oxygen species. This could be due to the reduction of the catalytic material.

The reactions could not be studied for longer period because after approx. 1 h, the pressure inside the reactor increased, brutally triggering the safety circuit of the setup and stopping the reaction. This could only be caused by an increase in the pressure drop due to severe carbon deposition in the catalyst bed.

The necessary production of water to close the mass balance and the brutal modification of the catalytic behavior after approx. one hour suggest that the catalysts undergo significant modifications during this period. Most probably, the NiO species are reduced to form metallic nickel, which is then responsible for the high carbon deposition. One would nevertheless expect that the activity and selectivity would progressively evolve, with carbon starting to be deposited as soon as nickel particles start being formed. On the contrary, the activity is rather stable during this reduction process, especially on Ni_3Cr-500, which, paradoxically, contains the largest amount of Ni. This suggests that the underlying $NiCr_2O_4$ phase can stabilize the metallic particles before it starts being reduced itself. At that moment, Ni particles may sinter rapidly and provoke sudden catalyst deactivation.

Given the evolution of the material during reaction, this catalytic behavior must be considered transient and cannot be extrapolated straightforwardly to a continuous DRM application. However, the selectivity towards syngas is remarkable at such low temperatures for the Ni_3Cr-500 catalyst. This opens the path for further investigation through adequate process conditions (e.g., by varying the CH_4/CO_2 composition) in order to slow the reduction of the material or through further investigation of material design and synthesis to better stabilize the active species. Another potential route to explore is the use of this material in non-steady state processes such as chemical looping reforming [39–43], or reaction–regeneration cyclic processes [44,45].

3. Materials and Methods

3.1. Chemicals

Nickel (II) nitrate hexahydrate ($Ni(NO_3)_2 \cdot 6H_2O$, ≥98%, Sigma Aldrich, St. Louis, MO, USA), chromium (III) nitrate nonahydrate ($Cr(NO_3)_3 \cdot 9H_2O$, ≥98%, Sigma Aldrich), iron (III) nitrate nonahydrate ($Fe(NO_3)_3 \cdot 9H_2O$, ≥98%, Sigma Aldrich, St. Louis, MO, USA), sodium hydroxide (NaOH, ≥98%, Sigma Aldrich), and sodium carbonate (Na_2CO_3, ≥98%, Sigma Aldrich, St. Louis, MO, USA) were used in LDH preparation. All reagents were analytical grade and used without any further purification. Distilled water was used in the synthesis and washing processes.

3.2. Catalyst Preparation

Ni_RFe and Ni_RCr LDH samples were prepared by coprecipitation method at constant pH at 70 °C with a divalent-to-trivalent cation molar ratio R of 2 and 3. These materials were denoted as Ni_2Cr, Ni_3Cr, Ni_2Fe, and Ni_3Fe LDHs. In a typical procedure, $Ni(NO_3)_2 \cdot 6H_2O$

and $Fe(NO_3)_3 \cdot 9H_2O$ were dissolved in distilled water to prepare a 1 M aqueous solution. Then, under vigorous stirring, $Ni(NO_3)_2$ (1M) and $Fe(NO_3)_3$ (1M) were dropped simultaneously (with Ni^{2+}/Fe^{3+} molar ratios in solution of 3:1 and 2:1) with an aqueous solution of NaOH on 100 mL of an aqueous solution of sodium carbonate. The pH during precipitation was maintained at a constant value of 10 by dropwise addition of NaOH solution at a temperature of 70 °C. After an aging step at this temperature for 24 h, the precipitates were recovered by filtration, washed several times with distilled water, and finally dried at 100 °C overnight in air. The same procedure was achieved to prepare Ni_RCr LDH. Finally, the dried LDH samples were subjected to calcination at 500 °C (heating rate of 5 °C/min) and held for 4 h. The calcined samples were labeled as Ni_2Fe-500, Ni_3Fe-500, Ni_2Cr-500, and Ni_3Cr-500 (500 refers to the applied calcination temperature).

3.3. Catalysts Characterization

Several physicochemical methods were used for the characterization of the catalysts before and after heating treatment.

Powder X-ray powder diffraction (PXRD) was performed using a Bruker AXS D8 Advance diffractometer (Bruker, Billerica, MA, USA) working in Bragg–Brentano geometry using Cu Kα radiation (λ = 1.54 Å), equipped with a LynxEye detector. Patterns were collected at room temperature, in the 2θ = 10–90° range, with a 0.02° step and 96 s counting time per step. The EVA software was used for phase identification. The average crystallite size (CS) is calculated from the line broadening of the most intense peak using Scherer's formula, $Cs = (0.9.\lambda)/(\beta \cos\theta)$, where (CS) is the average crystallite size, β is the half-maximum line width (FWHM), λ is the wavelength of radiation used (1.54056 Å), and θ is the angle of diffraction. X-ray diffraction at variable temperatures (HT-XRD) under an air atmosphere was carried out on the same apparatus equipped with XRK 900 chamber and a LynxEye detector. The patterns were collected every 25 °C, using a 0.1 °C/s heating rate between each temperature. The counting time being chosen to collect a diagram was set to 15 min in the 10–90° 2θ range. The sample was displayed on a platinum sheet. After measurement, the sample was cooled down to room temperature at a 0.3 °C/s cooling rate.

Thermogravimetry analysis (TGA) was performed on a SETARAM TG-92 (KEP Technologies, Caluire, France) thermobalance. The sample was heated at 5 °C/min in airflow conditions from 25 to 1000 °C. The released gases evolved during the analysis were monitored by a mass spectrometer (Pfeiffer Vacuum, Aßlar, Germany).

Laser-Raman spectra were recorded from 200 to 1500 cm^{-1} at room temperature using a FT-Raman spectrometer (Dilor XY Raman, Horiba France, Palaiseau, France) at an excitation wavelength of 647.1 nm, laser power of 3 mW, and spectral resolution of 0.5 cm^{-1}.

Attenuated Total Reflection Infra-Red spectra (IR-ATR) were recorded at room temperature using a Perkin Elmer model 400 (Perkin Elmer Inc., Waltham, MA, USA) in transmission mode, in the range from 350 to 4000 cm^{-1}.

The surface areas and pore size were calculated from N_2 adsorption–desorption isotherms measured on an ASAP 2020 (Micromeritics, Norcross, GA, USA) analyzer by Brunauer–Emmett–Teller (B.E.T) and Barret–Joyner–Halenda (B.J.H) methods.

XPS analyses were recorded using a Kratos Analytical Axis UltraDLD spectrometer (Kratos Analytical, Manchester, UK). The excitation was ensured by a monochromatic aluminum Kα source at 1486.6 eV operating at 180 W. The Kratos charge compensation system was applied to neutralize any charging effects. The residual pressure in the analysis chamber was below $5 \cdot 10^{-10}$ Torr. Survey scans were acquired at a pass energy of 160 eV with a 1 eV step, while core level spectra were acquired at 20 eV pass energy and with a 0.1 eV step. Data were processed using Casa XPS software. All spectra were calibrated using the C1s photoelectron peak corresponding to C-C bonds at 284.8 eV.

The reducible species which exist in the catalysts were profiled by temperature-programmed reduction. Hydrogen temperature-programmed reduction (H_2-TPR) was measured on a AutoChem II 2920 (Micromeritics, Norcross, GA, USA) apparatus with a thermal conductivity detector (TCD) to monitor the H_2 consumption. After calibration of

H_2 on the TCD, samples were sealed in a U-shaped quartz tube reactor and pre-treated in an argon atmosphere to remove surface impurities. Then, the temperature was raised from 25 to 1000 °C at 5 °C/min in a stream of 5% *v/v* H_2/Ar.

3.4. Catalytic Reforming Experiments

The tests of catalytic CO_2 reforming of methane were carried out at atmospheric pressure in a fixed-bed U -type quartz reactor. A 100 mg sample of catalyst was thoroughly mixed with SiC powder before loading in the reactor. The gas mixture containing CH_4:CO_2:He:Ar = 20:20:10:50 with a total flow of 100 mL/min was used, and the catalytic reaction was carried out in temperature-programmed mode from room temperature to 650 °C at a 5 °C/min heating rate. The gas flow was continuously monitored online using a Prisma 200 Pfeiffer mass spectrometer. Isothermal reactivity was performed using a new catalyst sample heated to reaction temperature (500 °C) in Argon and then exposed for approx. 1 h in the same reaction conditions.

4. Conclusions

Ni_RM (M = Cr or Fe, R = 2 or 3) hydrotalcite precursors were prepared using the coprecipitation method and were subsequently tested in the dry reforming of methane without any prior H_2 treatment. All the physicochemical characterization confirms the successful formation of the takovite structure. Upon calcination at 500 °C, Ni_RM hydrotalcites yielded stable mixed oxides consisting of a NiO phase and spinel structure ($NiCr_2O_4$ or $NiFe_2O_4$). Surface compositions evaluated by the XPS reveal different surface properties with Fe^{3+} species mainly at the surface of Ni_RFe systems and, in contrast, a balanced surface in Ni^{2+} and Cr^{3+} species for Ni_RCr catalysts. Ni_RCr catalysts are active and selective for DRM compared to Ni_RFe systems, showing the role of the trivalent metal on the structural and textural properties. Despite their high specific surface areas, the activity of Ni_RFe catalysts is low and can be attributed to (i) the localization of Fe^{3+} species on the surface and (ii) the loss of Ni-metal during the catalytic process, due to the formation of the Ni-Fe alloy favoring RWGS reaction. Ni_RCr catalysts show remarkable activity between 450 and 600 °C, in particular in terms of selectivity in such a low-temperature range. The deactivation of the catalysts at higher temperatures or after a long reaction time suggests a transient behavior associated with the reduction of NiO species to metallic Ni particles stabilized by the underlying $NiCr_2O_4$ phase or the presence of Cr_2O_3 oxide. During this process, the Ni particles remain active and selective until the $NiCr_2O_4$ start being reduced, provoking the sintering of the active phase. The remarkable properties of these partially reduced catalysts provide interesting perspectives for the use of these materials in non-steady state (looping or cycling) processes for methane valorization at particularly low temperatures for reforming reactions by CO_2.

Author Contributions: Conceptualization, R.B. and A.L.; Data curation, M.H.; Funding acquisition, R.B. and A.L.; Investigation, M.H., R.B., N.F.C., D.L., R.C., K.B., A.R., P.R., R.-N.V. and M.T.; Methodology, R.B. and A.L.; Supervision, R.B. and A.L.; Writing—original draft, M.H.; Writing—review and editing, M.H., R.B., N.F.C., D.L., R.C., K.B., A.R., P.R., R.-N.V., M.T. and A.L. All authors have read and agreed to the published version of the manuscript.

References

1. Tungatarova, S.; Xanthopoulou, G.; Vekinis, G.; Karanasios, K.; Baizhumanova, T.; Zhumabek, M.; Sadenova, M. Ni-Al Self-Propagating High-Temperature Synthesis Catalysts in Dry Reforming of Methane to Hydrogen-Enriched Fuel Mixtures. *Catalysts* **2022**, *12*, 1270. [CrossRef]
2. Pinheiro, A.L.; Pinheiro, A.N.; Valentini, A.; Filho, J.M.; Sousa, F.F.; Sousa, J.R.; Rocha, M.G.C.; Bargiela, P.; Oliveira, A.C. Analysis of coke deposition and study of the structural features of MAl_2O_4 catalysts for the dry reforming of methane. *Catal. Commun.* **2009**, *11*, 11–14. [CrossRef]
3. Crisafulli, C.; Scire, S.; Maggiore, R.; Minico, S.; Galvagno, S. CO_2 reforming of methane over Ni–Ru and Ni–Pd bimetallic catalysts. *Catal. Lett.* **1999**, *59*, 21–26. [CrossRef]
4. Wang, H.Y.; Ruckenstein, E. Carbon dioxide reforming of methane to synthesis gas over supported rhodium catalysts: The effect of support. *Appl. Catal. A-Gen.* **2000**, *204*, 143–152. [CrossRef]
5. Erdohelyi, A. Catalytic Reaction of Carbon Dioxide with Methane on Supported Noble Metal Catalysts. *Catalysts* **2021**, *11*, 159. [CrossRef]
6. Ruckenstein, E.; Hu, Y.H. Carbon dioxide reforming of methane over nickel/alkaline earth metal oxide catalysts. *Appl. Catal. A-Gen.* **1995**, *133*, 149–161. [CrossRef]
7. Rostrup-Nielsen, J.R.; Bak Hansen, J.H. CO_2-reforming of methane over transition metals. *J. Catal.* **1993**, *144*, 38–49. [CrossRef]
8. Bradford, M.C.J.; Vannice, M.A. CO_2 reforming of CH_4. *Catal. Rev.-Sci. Eng.* **1999**, *41*, 1–42. [CrossRef]
9. Rostrup-Nielsen, J.R. Production of synthesis gas. *Catal. Today* **1993**, *18*, 305–324. [CrossRef]
10. Wang, S.B.; Lu, G.Q. Carbon dioxide reforming of methane to produce synthesis gas over metal-supported catalysts: state of the art. *Energy Fuels* **1996**, *10*, 896–904. [CrossRef]
11. Romero, A.; Jobbagy, M.; Laborde, M.; Baronetti, G.; Amadeo, N. Ni(II)–Mg(II)–Al(III) catalysts for hydrogen production from ethanol steam reforming: Influence of the Mg content. *Appl. Catal. A-Gen.* **2014**, *47*, 398–404. [CrossRef]
12. Jin, L.; Xie, T.; Ma, B.; Li, Y.; Hu, H. Preparation of carbon-Ni/MgO-Al_2O_3 composite catalysts for CO_2 reforming of methane. *Int. J. Hydrog. Energy* **2017**, *42*, 5047–5055. [CrossRef]
13. Roussel, H.; Briois, V.; Elkaim, E.; De Roy, A.; Besse, J.P.; Jolivet, J.P. Study of the Formation of the layered double hydroxide [Zn−Cr−Cl]. *Chem. Mater.* **2001**, *13*, 329–337. [CrossRef]
14. You, Y.; Zhao, H.; Vance, G.F. Hybrid organic–inorganic derivatives of layered double hydroxides and dodecylbenzenesulfonate: Preparation and adsorption characteristics. *J. Mater. Chem.* **2002**, *12*, 907–912. [CrossRef]
15. Chatla, A.; Almanassra, I.W.; Kochkodan, V.; Laoui, T.; Alawadhi, H.; Atieh, M.A. Efficient Removal of Eriochrome Black T (EBT) Dye and Chromium (Cr) by Hydrotalcite-Derived Mg-Ca-Al Mixed Metal Oxide Composite. *Catalysts* **2022**, *12*, 1247. [CrossRef]
16. Triantafyllidis, K.S.; Peleka, E.N.; Komvokis, V.G.; Mavros, P.P. Iron-modified hydrotalcite-like materials as highly efficient phosphate sorbents. *J. Colloid Interface Sci.* **2010**, *342*, 427–436. [CrossRef]
17. Frost, R.; Jagannadha-Reddy, B. Thermo-Raman spectroscopic study of the natural layered double hydroxide manasseite. *Spectrochim. Acta A Mol. Biomol. Spectrosc.* **2006**, *65*, 553–559. [CrossRef]
18. Borromeo, L.; Zimmermann, U.; Andò, S.; Coletti, G.; Bersani, D.; Basso, D.; Gentile, P.; Schulz, B.; Garzanti, E. Raman spectroscopy as a tool for magnesium estimation in Mg-calcite. *J. Raman Spectrosc.* **2017**, *48*, 983–992. [CrossRef]
19. Benrabaa, R.; Boukhlouf, H.; Löfberg, A.; Rubbens, A.; Vannier, R.N.; Bordes-Richard, E.; Barama, A. Nickel ferrite spinel as catalyst precursor in the dry reforming of methane: Synthesis, characterization and catalytic properties. *J. Nat. Gas Chem.* **2012**, *21*, 595–604. [CrossRef]
20. Kreisel, J.; Lucazeau, G.; Vincent, H. Raman Spectra and Vibrational Analysis of $BaFe_{12}O_{19}$ Hexagonal Ferrite. *J. Sol. State Chem.* **1998**, *137*, 127–137. [CrossRef]
21. Faid, A.Y.; Barnett, A.O.; Seland, F.; Sunde, S. Ni/NiO nanosheets for alkaline hydrogen evolution reaction: In situ electrochemical-Raman study. *Electrochim. Acta* **2020**, *361*, 137040. [CrossRef]
22. Colomban, P.; Jullian, S.; Parlier, M.; Monge-Cadet, P. Identification of the high-temperature impact/friction of aeroengine blades and cases by micro Raman spectroscopy. *Aerosp. Sci. Technol.* **1999**, *3*, 447–459. [CrossRef]

23. Singh, J.; Kumar, R.; Vermaa, V.; Kumar, R. Role of Ni^{2+} substituent on the structural, optical and magnetic properties of chromium oxide ($Cr_{2-x}Ni_xO_3$) nanoparticles. *Ceram. Int.* **2020**, *46*, 24071–24082. [CrossRef]

24. Olszówka, E.; Karcz, R.; Bielańska, E.; Kryściak-Czerwenka, J.; Napruszewska, D.; Sulikowski, B.; Socha, P.; Gaweł, A.; Bahranowski, K.; Olejniczak, Z.; et al. New insight into the preferred valency of interlayer anions in hydrotalcitelike compounds: The effect of Mg/Al ratio. *Appl. Clay Sci.* **2018**, *155*, 84–94. [CrossRef]

25. Rozov, K.; Berner, U.; Taviot-Gueho, T.; Leroux, F.; Renaudin, G.; Kulil, D.; Diamond, L.W. Synthesis and characterization of the LDH hydrotalcite–pyroaurite solid-solution series. *Cem. Concr. Res.* **2010**, *40*, 1248–1254. [CrossRef]

26. Benito, P.; Labajos, F.M.; Rives, V. Microwave-treated layered double hydroxides containing Ni^{2+} and Al^{3+}: The effect of added Zn^{2+}. *J. Solid State Chem.* **2006**, *179*, 3784–3797. [CrossRef]

27. Kovanda, F.; Rojka, T.; Bezdicka, P.; Jiratova, K.; Obalova, L.; Pacultova, K.; Bastl, Z.; Grygar, T. Effect of hydrothermal treatment on properties of Ni–Al layered double hydroxides and related mixed oxides. *J. Solid State Chem.* **2009**, *182*, 27–36. [CrossRef]

28. Shebanova, O.N.; Lazor, P. Raman spectroscopic study of magnetite ($FeFe_2O_4$): A new assignment for the vibrational spectrum. *J. Solid State Chem.* **2003**, *174*, 424–430. [CrossRef]

29. Graves, P.R.; Johnston, C.; Campaniello, J.J. Raman scattering in spinel structure ferrites. *Mat. Bul Res.* **1988**, *23*, 1651–1660. [CrossRef]

30. D'Ippolito, V.; Andreozzi, G.B.; Bersani, D.; Lotticib, P.P. Raman fingerprint of chromate, aluminate and ferrite spinels. *J. Raman Spectrosc.* **2015**, *46*, 1255–1264. [CrossRef]

31. Hyun-Kim, J.; Soon- Hwang, I. Development of an in situ Raman spectroscopic system for surface oxide films on metals and alloys in high temperature water. *Nucl. Eng. Des.* **2005**, *235*, 1029–1040. [CrossRef]

32. Takehira, K.; Kawabata, T.; Shishido, T.; Murakami, K.; Ohi, T.; Shoro, D.; Honda, M.; Takaki, K. Mechanism of reconstitution of hydrotalcite leading to eggshell-type Ni loading on Mg–Al mixed oxide. *J. Catal.* **2005**, *231*, 92–104. [CrossRef]

33. X-ray Photoelectron Spectroscopy (XPS) Reference Pages. Available online: http://www.xpsfitting.com/ (accessed on 1 September 2022).

34. Biesingera, M.C.; Payne, B.P.; Grosvenor, A.P.; Laua, L.W.M.; Gerson, A.R.; Smart, R.S.C. Resolving surface chemical states in XPS analysis of first row transition metals, oxides and hydroxides: Cr, Mn, Fe, Co and Ni. *Appl. Surf. Sci.* **2011**, *257*, 2717–2730. [CrossRef]

35. Hosseini, S.A.; Alvarez-Galvan, M.C.; Fierro, J.L.G.; Niaei, A.; Salari, D. MCr2O4 (M=Co, Cu, and Zn) nanospinels for 2-propanol combustion: Correlation of structural properties with catalytic performance and stability. *Ceram. Int.* **2013**, *39*, 9253–9261. [CrossRef]

36. Rouibah, K.; Barama, A.; Benrabaa, R.; Guerrero-Caballero, J.; Kane, T.; Vannier, R.N.; Rubbens, A.; Löfberg, A. Dry reforming of methane on nickel-chrome, nickel-cobalt and nickel-manganese catalysts. *Int. J. Hydrogen Energy* **2017**, *42*, 29725–29734. [CrossRef]

37. Benrabaa, R.; Aissat, F.; Fodil Cherif, N.; Gouasmia, A.; Yeste, P.; Cauqui, M.A. Catalytic oxidation of carbon monoxide over CeO_2 and La_2O_3 oxides supported nickel catalysts: The effect of the support and NiO loading. *ChemistrySelect* **2022**, *7*, 104–133. [CrossRef]

38. Benrabaa, R.; Löfberg, A.; Rubbens, A.; Bordes-Richard, E.; Vannier, R.N.; Barama, A. Structure, reactivity and catalytic properties of nanoparticles of nickel ferrite in the dry reforming of methane. *Catal. Today* **2013**, *203*, 188–195. [CrossRef]

39. Bhavsar, S.; Najera, M.; Solunke, R.; Veser, G. Chemical looping: To combustion and beyond. *Catal. Today* **2014**, *228*, 96–105. [CrossRef]

40. Bhavsar, S.; Veser, G. Chemical looping beyond combustion: Production of synthesis gas via chemical looping partial oxidation of methane. *RSC Adv.* **2014**, *4*, 47254–47267. [CrossRef]

41. Galvita, V.; Poelman, H.; Detavernier, C.; Marin, G. Catalyst-assisted chemical looping for CO_2 conversion to CO. *Appl. Catal. B Environ.* **2015**, *164*, 184–191. [CrossRef]

42. Löfberg, A.; Guerrero-Caballero, J.; Kane, T.; Rubbens, A.; Jalowiecki-Duhamel, L. Ni/CeO_2 based catalysts as oxygen vectors for the chemical looping dry reforming of methane for syngas production. *Appl. Catal. B Environ.* **2017**, *212*, 159–174. [CrossRef]

43. Löfberg, A.; Guerrero-Caballero, J.; Kane, T.; Jalowiecki-Duhamel, L. Chemical looping dry reforming of methane: Toward shale-gas and biogas valorization. *Chem. Eng. Process. Process Intensif.* **2017**, *122*, 523–529. [CrossRef]

44. Tang, M.; Xu, L.; Fan, M. Progress in oxygen carrier development of methane-based chemical-looping reforming: A review. *Appl. Energy* **2015**, *151*, 143–156. [CrossRef]

45. Assabumrungrat, S.; Charoenseri, S.; Laosiripojana, N.; Kiatkittipong, W.; Praserthdam, P. Effect of oxygen addition on catalytic performance of Ni/SiO_2-MgO toward carbon dioxide reforming of methane under periodic operation. *Int. J. Hydrogen Energy* **2009**, *34*, 6211–6220. [CrossRef]